

Evolution of electronic correlations across the rutile, perovskite, and Ruddlesden-Popper iridates with octahedral connectivity

Jason K. Kawasaki,^{1,2,3,*} Masaki Uchida,⁴ Hanjong Paik,² Darrell G. Schlom,^{2,3} and Kyle M. Shen^{1,3,†}

¹Laboratory for Atomic and Solid State Physics, Cornell University, Ithaca, New York 14853, USA

²Department of Materials Science and Engineering, Cornell University, Ithaca, New York 14853, USA

³Kavli Institute at Cornell for Nanoscale Science, Cornell University, Ithaca, New York 14853, USA

⁴Department of Applied Physics, University of Tokyo, Tokyo, Japan

(Received 30 May 2016; revised manuscript received 19 July 2016; published 6 September 2016)

The confluence of electron correlations and spin-orbit interactions is critical to realizing quantum phases in $5d$ transition metal oxides. Here, we investigate how the strength of the effective electron correlations evolve across a series of d^5 iridates comprised of IrO_6 octahedra, ranging from the layered correlated insulator Sr_2IrO_4 , to the three-dimensional perovskite semimetal SrIrO_3 , to metallic rutile IrO_2 in which the octahedra are arranged in a mixed edge and corner sharing network. Through a combination of reactive oxide molecular-beam epitaxy, *in situ* angle-resolved photoemission spectroscopy, core level photoemission, and density functional theory, we show how the effective electron correlations weaken as a function of increasing connectivity of the IrO_6 network and p - d hybridization. Our results demonstrate how structure and connectivity can be used to control the strength of correlations in the iridates.

DOI: [10.1103/PhysRevB.94.121104](https://doi.org/10.1103/PhysRevB.94.121104)

Electron-electron correlations play an essential role in renormalizing the ground state of many transition metal oxides. While this renormalization was once thought to be weak in the late transition metals due to the extended spatial extent of $5d$ orbitals, it is now well appreciated that spin-orbit coupling can enhance the effects of correlations, particularly in the case of iridium oxides. A prime example is that of Sr_2IrO_4 , for which band theory predicts a metallic ground state, but the combination of spin-orbit coupling and correlations give rise to an antiferromagnetic $J_{\text{eff}} = 1/2$ insulator [1]. This combination of spin-orbit coupling and correlations has proven key to the physics of proposed states in the iridates, including superconductivity [2–5], the Kitaev model [6], the Weyl semimetal [7–9], and other topological states [10,11].

The majority of these exotic states have been typically proposed for iridates in the perovskite $A\text{IrO}_3$ [10–13], layered Ruddlesden-Popper $A_{n+1}\text{Ir}_n\text{O}_{3n+1}$ [1,14–16], and pyrochlore $A_2\text{Ir}_2\text{O}_7$ [9,17] structures, where A is an alkaline earth metal. These different crystal structures share as a common building block IrO_6 octahedra where the Ir^{4+} is in a $5d^5$ configuration. For example, SrIrO_3 is a material in which the octahedra form a three-dimensional corner sharing network and is proposed to be a topological crystalline insulator with line nodes protected by crystal symmetry [10,11]. Sr_2IrO_4 is composed of a two-dimensional octahedral network and is proposed to be a $J_{\text{eff}} = 1/2$ superconductor upon electron doping [2–5]. Another material which shares the same IrO_6 ($5d^5$) building block is the rutile polymorph of IrO_2 . In the perovskite, Ruddlesden-Popper, and pyrochlore structures, the IrO_6 octahedra are connected in exclusively corner-sharing networks, whereas in the rutile structure, the octahedra exhibit a higher degree of connectivity and are instead tiled with a mixture of both corner and edge sharing neighbors [Fig. 1(a)].

IrO_2 exhibits a number of properties that make it fundamentally interesting and technologically relevant, particularly for spintronic applications. These include novel magnetotransport properties, with a large spin Hall angle which clearly highlights the importance of spin-orbit coupling [18], as well as a Hall effect whose carrier sign can be switched by changing the orientation of the external magnetic field [19]. In addition, IrO_2 is a very promising catalyst for the oxygen evolution reaction [20,21]. Given its similar *local* structure, one might expect IrO_2 to share many of the same properties as the other iridates. On the other hand, it is known that subtle structure distortions, such as octahedral tilts, can dramatically alter the properties of complex oxides in general [22], and perovskite iridates in particular [13]. Therefore, the precise role of electron correlations in determining the properties across iridates with different connectivity remains an open question.

In this Rapid Communication, we investigate how the strength of the effective correlations across the iridates varies with the connectivity of the IrO_6 octahedra using a combination of reactive oxide molecular-beam epitaxy (MBE) synthesis, *in situ* angle-resolved photoemission spectroscopy (ARPES), core level spectroscopy, and density functional theory. In surprising contrast to Sr_2IrO_4 and SrIrO_3 , we find that electron-electron correlations are unusually weak in IrO_2 , surprising for a transition metal oxide. We discover that the combination of increasing the octahedral connectivity, the metal-oxygen covalency, and the metal-metal interactions reduce the effective correlation strength when going from the antiferromagnetic Mott insulator Sr_2IrO_4 to Fermi liquid IrO_2 , which does not exhibit any appreciable mass enhancement. Thin films of (001) SrIrO_3 , Sr_2IrO_4 , and (110) IrO_2 were grown by MBE on $(\text{LaAlO}_3)_{0.29}(\text{SrAl}_{0.5}\text{Ta}_{0.5}\text{O}_3)_{0.71}$ (LSAT) (001) substrates (SrIrO_3 , Sr_2IrO_4) and TiO_2 (110) substrates (IrO_2). The films were grown under a background partial pressure of 10^{-6} torr of distilled ozone at a substrate temperature of 900°C for Sr_2IrO_4 , 650°C for SrIrO_3 , and 350°C for IrO_2 . Additional details about the growth and characterization of SrIrO_3 and Sr_2IrO_4 can be found in Ref. [13]. X-ray diffraction (XRD,

*Current address: Department of Materials Science and Engineering, University of Wisconsin, Madison WI 53706.

†kshen@cornell.edu

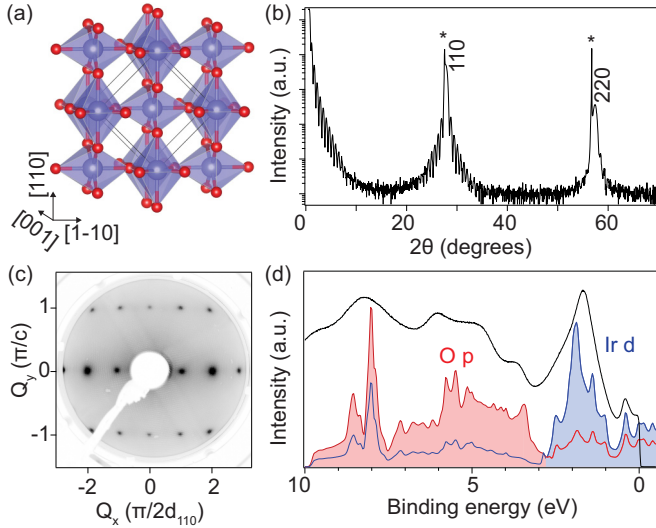


FIG. 1. Crystal structure and valence bands of IrO₂ (110) films. (a) Crystal structure of rutile, showing chains of edge sharing IrO₆ octahedra oriented along the *c* [001] axis. Ir atoms are in blue, O atoms in red. (b) XRD 2θ scan of epitaxial IrO₂ on a TiO₂ (110) substrate. Substrate peaks are marked by asterisks. (c) Low energy electron diffraction pattern of the IrO₂ (110) surface measured at 100 eV. (d) Momentum-integrated valence band spectrum [black curve, $k = (1,0) - (1,1)$] and comparison to GGA+SO partial density of states (shaded).

Cu $K\alpha$) θ - 2θ scans confirmed that the IrO₂ was epitaxial with an out-of-plane d_{110} spacing of 3.20(4) Å [near the bulk value of 3.181 Å [23], Fig. 1(b)], and have sharp rocking curves (Supplemental Material [24]). The presence of sharp Kiessig fringes in the XRD pattern indicates that the film was smooth with a thickness of 16 nm, in agreement with RHEED oscillations. Following growth, samples were transferred through an ultrahigh vacuum manifold ($<3 \times 10^{-10}$ torr) for ARPES measurements which were performed using a VG Scienta R4000 analyzer. For IrO₂ and Sr₂IrO₄, density functional theory calculations were performed using the generalized gradient approximation including fully relativistic SOC (GGA+SO) in WIEN2K [25]. Our calculations are in agreement with a previous DFT+DMFT study [26]. For SrIrO₃, calculations were performed within the local density approximation including spin orbit interaction (LDA+SO) using OPENMX as described in Ref. [13].

We begin with rutile IrO₂, where each O is coordinated to three Ir nearest neighbors. In Fig. 1(d), we show the valence band of IrO₂ using He II photons ($h\nu = 40.8$ eV) compared to the calculated density of states. The peaks between E_F and 3 eV binding energy are of primarily Ir t_{2g} character, while the broad bands between 3 and 10 eV are predominantly O $2p$ orbitals. The occupied t_{2g} bandwidth of 3 eV for IrO₂ is significantly broader than that of SrIrO₃ and Sr₂IrO₄ (approximately 0.3 and 0.8 eV, respectively [13]). Each of the major features in the measured spectrum is remarkably well reproduced by the DFT calculation, and consistent with a previous hard x-ray photoemission study [27], but with a higher sensitivity to the O $2p$ states due to the higher relative cross section at low photon energies.

The low-energy electronic structure of IrO₂ is shown in Fig. 2, measured using He I α photons ($h\nu = 21.2$ eV), where the energy dispersion curves (EDCs) show sharp quasiparticle (QP) peaks. The dispersion is highly anisotropic and dominated by hole pockets centered at (2,0) [(0,0) and (1,1), consistent with previous magnetotransport measurements [19]. Given that the peaks in the EDCs are well fit by a Lorentzian line shape, the widths of the momentum distribution curves (MDCs) exhibit an ω^2 dependence, and the resistivity exhibits a T^2 dependence at low temperatures [28]; these findings indicate that IrO₂ is well described by a Fermi liquid ground state. To better quantify the strength of the electron-electron correlations, we compare our experimentally extracted dispersions with GGA+SO calculations (excluding any onsite Coulomb repulsion U). We find remarkable agreement between our extracted dispersions and GGA+SO, in terms of the Fermi velocity (v_F), the Fermi wave vector (k_F), and the full occupied bandwidth [Fig. 2(b)]. Comparing v_F for the hole pockets at $k = (2,0)$ and (1,1) yields no observable renormalization $v_{F,\text{DFT}}/v_F = 1.0 \pm 0.1$. Furthermore, the measured occupied bandwidth throughout the Brillouin zone is within ten percent of the DFT values at binding energies extending to larger than 1 eV. This level of quantitative agreement between experiment and DFT is remarkable in transition metal oxides, where typically $m^*/m_{\text{DFT}} \approx 2-6$, in material families such as cuprates, nickelates, manganites, titanates, ruthenates, and other iridates [29–34]. From EDC fits of the QP peak, we extract an effective quasiparticle residue of $Z' = 0.9 \pm 0.1$ (Supplemental Material [24]), in good agreement with the lack of appreciable velocity renormalization. For comparison, in Sr₃Ir₂O₇, $Z' = 0.25-0.5$ [16]. These findings are also consistent with the relatively small Sommerfeld coefficient of $\gamma = 0.67$ mJ/(mol \cdot K²) for IrO₂ bulk crystals [35], which is comparable in magnitude to that of simple elemental transition metals.

Comparisons between measurements taken with He I α (21.2 eV) and He II α (40.8) eV were performed to accurately determine the out-of-plane momentum to be $k_z = (0.76 \pm 0.05)\pi/d_{110}$, corresponding to an inner potential of $U_0 = 11.5$ eV (Supplemental Material [24]), a value typical for oxides ($U_0 = 9$ to 15 eV [13,36–38]). In Fig. 2(b) (bottom), we show a simulation of the ARPES spectra at $k_z = 0.76\pi/d_{110}$ with a smearing of $\Delta k_z = 1/\lambda$ ($\lambda \approx 4$ Å is the finite escape depth) and an imaginary self energy broadening of $Im(\Sigma) = 0.05 + 0.3\omega^2$ eV. The simulation bears a remarkable resemblance to the raw ARPES data in Fig. 2(b) (top), once again suggesting weak electron correlations in IrO₂. Along (1,0) – (1,1), some discrepancies can be observed which we attribute to rapidly dispersing features in k_z (Supplemental Material, Fig. S3 [24]) which are not fully captured by the k_z smearing. We also observe two features that are not readily apparent in the GGA+SO calculations, namely a second hole pocket and deep electron pocket with band minimum near 0.4 eV along (1,1) – (2,1), which may arise from surface-derived features.

We now compare the effective correlation strength in IrO₂ to other iridates with decreasing connectivity: the perovskite SrIrO₃ (2 Ir atoms coordinated to each O) and layered Sr₂IrO₄ (1.5 Ir atoms coordinated to each O). ARPES measurements and extracted dispersions for all three materials are shown in

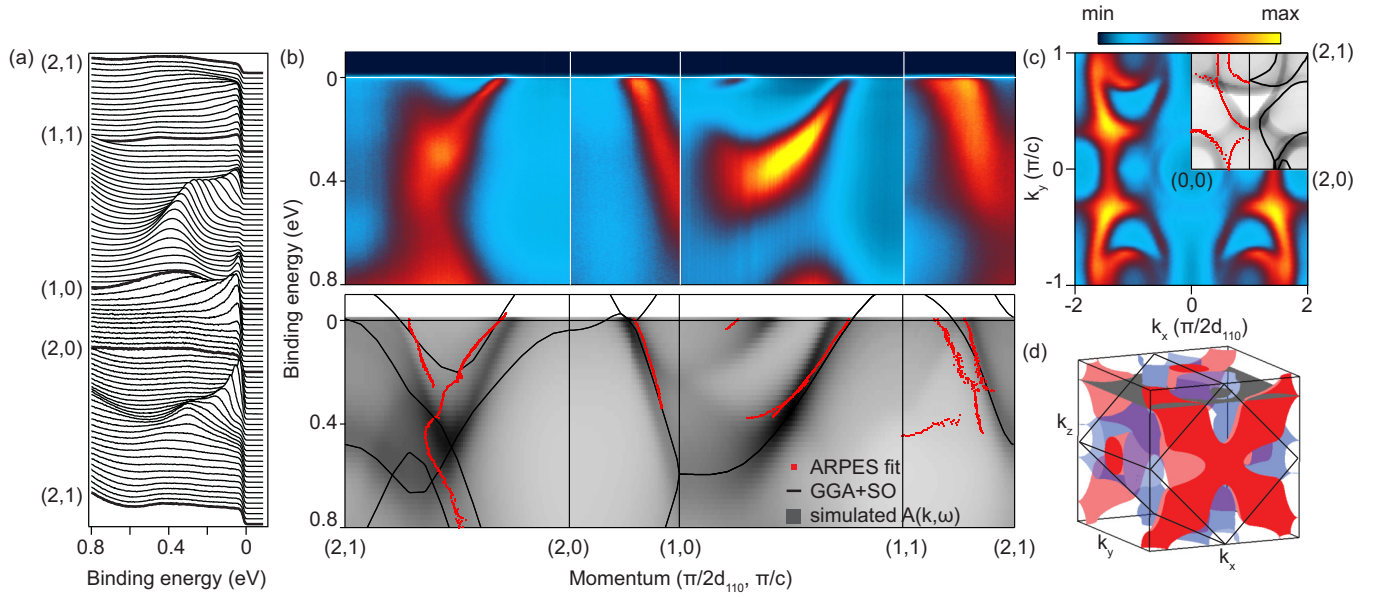


FIG. 2. (a) Energy dispersion curves (EDCs) showing sharp quasiparticle peaks. We define our axes such that $k_x \parallel [1\bar{1}0]$ and $k_y \parallel [001]$, and hence the high symmetry points are expressed in units of $(\pi/2d_{110}, \pi/c)$. (b) False-color ARPES intensity (top) and comparison of the extracted dispersions with theory (bottom), for GGA+SO at fixed k_z and for a simulated spectral intensity with k_z smearing and lifetime broadening (grayscale). (c) ARPES Fermi surface (color scale), corresponding approximately to a slice through the three-dimensional Fermi surface at constant k_z . The upper right quadrant shows the extracted Fermi surface (red dots) along with the GGA+SO Fermi surface (black lines) and a k_z broadened simulation (grayscale). (d) Three-dimensional Fermi surface.

Fig. 3, along with comparison to DFT+SO calculations. As described earlier, in IrO_2 the bandwidth and Fermi velocity do not exhibit observable signs of renormalization compared to the calculation ($v_{F,\text{DFT}}/v_{F,\text{ARPES}} = 1 \pm 0.1$), while in SrIrO_3 the effective mass of the (1,0) inner hole pocket is renormalized by a factor of $m^*/m_{\text{DFT}} = 2.0 \pm 0.2$, and in Sr_2IrO_4 , DFT+SO does not predict the Mott insulating ground state. Additionally, we find that the bandwidth for Sr_2IrO_4 is renormalized by a factor $W/W_{\text{DFT}} = 1.35$. This suggests a clear evolution in the effective correlation strength across the iridates as a function of the connectivity of the IrO_6 octahedra, whose trend is plotted in Fig. 4(c) (black circles). In all cases, the films were thicker than 40 monolayers, much larger than the Thomas-Fermi screening length, and did not have a polar discontinuity at the film/substrate interface. Hence quantum confinement or

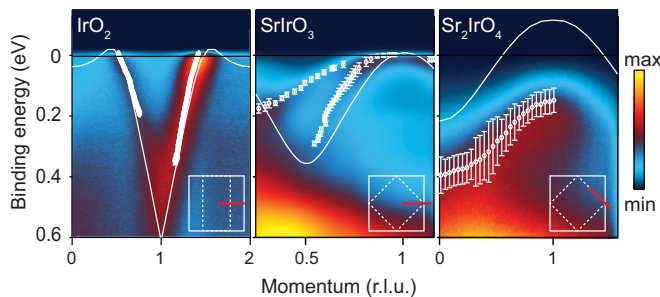


FIG. 3. ARPES intensity (color scale), extracted dispersions (white circles), and DFT+SO (white lines) showing increasing renormalizations from IrO_2 to SrIrO_3 and Sr_2IrO_4 . Momenta are expressed in units of $\pi/2d_{110}$, π/a , and $\sqrt{2}\pi/a$, respectively. The SrIrO_3 and Sr_2IrO_4 data are adapted from Ref. [13].

interfacial effects are expected to be negligible, and thus the ARPES measurements are expected to be comparable to results from a cleaved single crystal.

In addition to the low energy electronic structure measured by ARPES, we also observe systematic changes across the iridates in the $\text{Ir } 4f_{5/2}$ and $4f_{7/2}$ core levels measured *in situ* using $\text{Al K}\alpha$ [$h\nu = 1486.3$ eV, Fig. 4(a)]. In all of the iridates, a multicomponent peak structure is observed, which arises from a sharp screened $4f$ doublet (red) and a broader unscreened doublet (blue), which appears at higher binding energy. The relative ratio between the unscreened and screened core levels has been employed as a proxy for measuring the effective strength of correlations across the ruthenates [39]. In our fits, we use a conventional Shirley background (dotted), two Voigt components for each $4f$ doublet, and a Doniac Sunjic asymmetry parameter to account for the interaction between the core hole and the Fermi sea in metallic IrO_2 . We constrain the ratio of the $4f_{5/2}$ to $4f_{7/2}$ weights within each doublet and constrain the spin-orbit splitting to known values. Hence the only free parameters are the relative intensities of the components, their lifetimes, and their binding energy shifts (Supplemental Material, Table I [24]). In IrO_2 , we find that the $4f$ core levels are dominated by the sharp screened peak with a relatively small contribution from the unscreened component, also consistent with x-ray photoemission measurements of IrO_2 and RuO_2 [27,40]. Moving to SrIrO_3 and Sr_2IrO_4 , the weight of the screened component decreases while the relative weight of the unscreened component increases; in Sr_2IrO_4 the spectra are dominated by the unscreened component. This trend is summarized versus octahedral connectivity in Fig. 4(c).

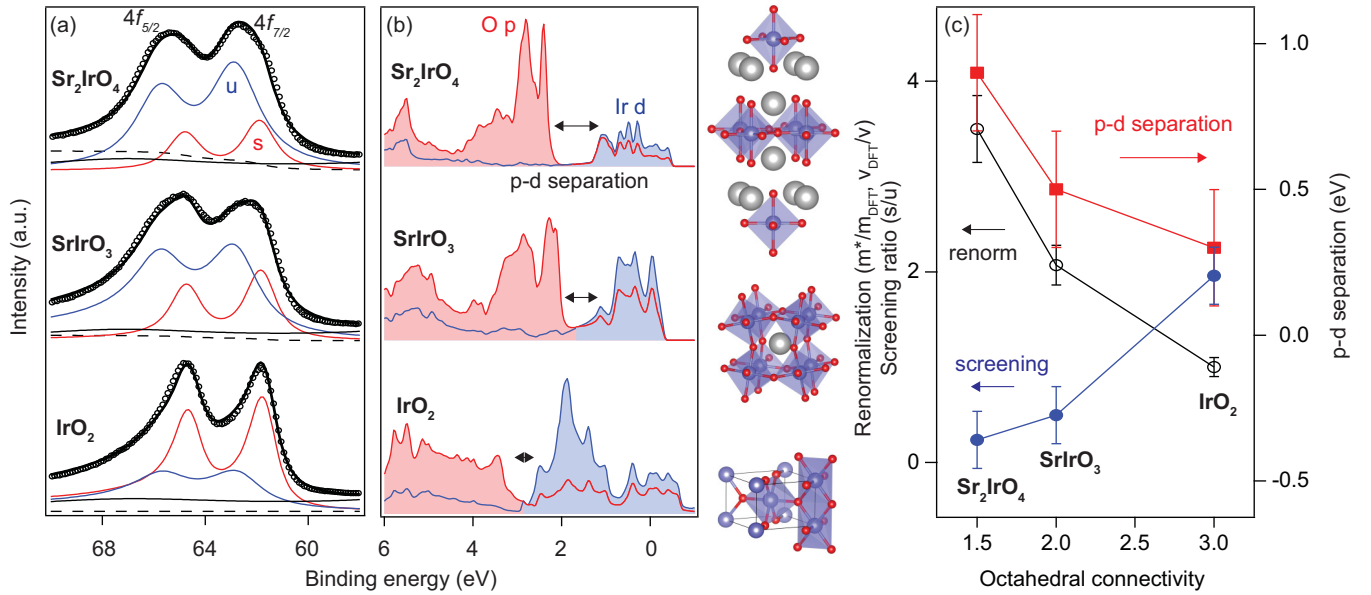


FIG. 4. The connection between structure and correlations across the iridates. (a) Comparison of the Ir $4f$ and $5p$ core levels (measurement, open circles), showing screened (s, red) and unscreened (u, blue) $4f$ components, along with a broad $5p_{1/2}$ (black). (b) Comparison of the DFT+SO PDOS. The corresponding crystal structures for Sr_2IrO_4 , SrIrO_3 , and IrO_2 are shown at the right. (c) Renormalization, Ir $4f$ screening ratio, and p - d hybridization versus octahedral connectivity (average number of Ir nearest neighbors coordinated to each oxygen). For the IrO_2 and SrIrO_3 renormalizations we use the velocity ($v_{F,\text{DFT}}/v_F$) and mass (m^*/m_{DFT}) renormalizations, respectively, from our ARPES and DFT+SO. For Sr_2IrO_4 , due to the lower statistics of the ARPES measurement we use the mass renormalization from DMFT [31].

Having established how correlations evolve across the iridates, we now investigate its possible origins. In the DFT+SO densities of states [Fig. 4(b)], the width of the occupied Ir t_{2g} bands increases when moving from two-dimensional Sr_2IrO_4 ($W \approx 1$ eV), to three-dimensional corner sharing SrIrO_3 , to three-dimensional edge and corner sharing IrO_2 ($W \approx 3$ eV), which one can consider as a hyperconnected variant of the perovskite structure composed of the same IrO_6 octahedral building block. Thus, with increasing W , the ratio U/W decreases making the effective correlations in IrO_2 smaller. Furthermore, in Sr_2IrO_4 , the density of states exhibits a clear gap (≈ 0.9 eV) separating the Ir $5d$ and O $2p$ orbitals [Fig. 4(b)], indicative of a more ionic character, where the conventional picture of oxygen mediated hoppings between the transition metal sites is valid. In this case, the correlations, in conjunction with the spin-orbit coupling, are strong enough to turn the system into a Mott insulator (Fig. 3). In SrIrO_3 , the density of states shows a small overlap between the p and d states and a reduced separation of ≈ 0.5 eV (defined as the separation using a tangent line extrapolation to zero of the leading edges of the p and d states, see Supplemental Material [24]), consistent with semimetallic SrIrO_3 having weaker effective correlations than Mott insulating Sr_2IrO_4 . Finally, in metallic IrO_2 , the density of states shows a further reduction of the p - d separation (≈ 0.3 eV) and increased overlap between p and d states. This leads to a more covalent character, which is also evidenced in tight-binding models, for which metal-oxygen covalency parameters are crucial to reproducing the electronic structure of RuO_2 and IrO_2 [41]. This covalent hybridization leads to a reduced effective correlation strength, as the spectral weight is shifted onto the more weakly correlated oxygen $2p$ orbitals as opposed to the more strongly correlated transition

metal d orbitals, thereby resulting in a weaker effective renormalization for IrO_2 . These trends are also consistent with the Zaanen-Sawatzky-Allen picture [42], in which the size of the Mott or charge transfer gap is determined by a balance between the on-site Coulomb repulsion U , the p - d separation Δ_{p-d} , and the p - d hybridization interaction T . Although the bare atomic component of the on-site Coulomb repulsion U should remain largely constant across the iridates, the screened component of U is decreased by the increased p - d covalency in IrO_2 . We argue that this p - d covalency, as described by Δ_{p-d} and T , is in turn strongly determined by the octahedral connectivity. Finally for IrO_2 , there is also significant direct bonding between the Ir sites, which is largely insignificant for Sr_2IrO_4 and SrIrO_3 , which provides an additional hopping channel in IrO_2 , as also suggested from a molecular orbital picture proposed for the rutile structure at d^5 filling [43].

A summary of how the low-energy mass (velocity) renormalization (m^*/m_{DFT} , $v_{F,\text{DFT}}/v_F$ open black circles), the $4f$ core hole screening (ratio of screened to unscreened doublets, closed blue circles), and the p - d separation (red squares) vary as a function of the IrO_6 octahedral connectivity (the average number of Ir nearest neighbors connected to each oxygen), is shown in Fig. 4(c). We find that each of these parameters depends strongly on the structure as parameterized by the octahedral connectivity: The connectivity determines the degree of ionic versus covalent bonding, which in turn determines the correlation induced renormalization and degree of metallicity. Hence the low energy electronic structure of the iridates is not simply set by the local parameters of spin-orbit coupling, band filling, and crystal field splitting alone, but is highly dependent on the octahedral tiling structure in which a high degree of connectivity leads to deviations from the atomic

limit, with stronger covalent character and reduced effective correlations. Conversely, recent experimental and theoretical studies suggest in $5d$ transition metal oxide and fluoride systems with nearly isolated octahedra and thus much narrower bandwidths, the correlations are enhanced, approaching the more idealized $J_{\text{eff}} = 1/2$ limit [44,45].

In summary, using a combination of MBE, *in situ* ARPES, core level spectroscopy, density functional calculations, and choosing the $5d^5$ iridates as a model system, we revealed how electron correlations evolve dramatically as a function of octahedral connectivity, from a correlated $J_{\text{eff}} = 1/2$ Mott insulator in Sr_2IrO_4 , to a nearly uncorrelated metal in rutile IrO_2 , and believe this can be generalized across different

transition metal oxide families. The ability to accurately quantify the strength of electron correlations should provide important inputs and design considerations for engineering potential correlated electronic materials in artificial correlated materials and heterostructures.

We thank T. Birol, C. Fennie, C. H. Kim, and Y. F. Nie for fruitful discussions. This work was supported the Air Force Office of Scientific Research (Grants No. FA9550-12-1-0335 and FA2386-12-1-3103) and the Office of Naval Research (Grant No. N00014-12-1-0791). This work made use of the Cornell Center for Materials Research Shared Facilities which are supported through the NSF MRSEC program (DMR-1120296).

-
- [1] B. J. Kim, H. Jin, S. J. Moon, J.-Y. Kim, B.-G. Park, C. S. Leem, J. Yu, T. W. Noh, C. Kim, S.-J. Oh *et al.*, *Phys. Rev. Lett.* **101**, 076402 (2008).
- [2] F. Wang and T. Senthil, *Phys. Rev. Lett.* **106**, 136402 (2011).
- [3] Y. K. Kim, O. Krupin, J. D. Denlinger, A. Bostwick, E. Rotenberg, Q. Zhao, J. F. Mitchell, J. W. Allen, and B. J. Kim, *Science* **345**, 187 (2014).
- [4] Y. K. Kim, N. H. Sung, J. D. Denlinger, and B. J. Kim, *Nat. Phys.* **12**, 37 (2015).
- [5] Y. J. Yan, M. Q. Ren, H. C. Xu, B. P. Xie, R. Tao, H. Y. Choi, N. Lee, Y. J. Choi, T. Zhang, and D. L. Feng, *Phys. Rev. X* **5**, 041018 (2015).
- [6] S. H. Chun, J.-W. Kim, H. Z. Jungho Ki, C. C. Stoumpos, C. D. Malliakas, J. F. Mitchell, K. Mehlawat, Y. Singh, Y. Choi, T. Gog *et al.*, *Nat. Phys.* **11**, 462 (2015).
- [7] W. Witczak-Krempa, G. Chen, Y. B. Kim, and L. Balents, *Annu. Rev. Condens. Matter Phys.* **5**, 57 (2014).
- [8] L. Savary, E.-G. Moon, and L. Balents, *Phys. Rev. X* **4**, 041027 (2014).
- [9] X. Wan, A. M. Turner, A. Vishwanath, and S. Y. Savrasov, *Phys. Rev. B* **83**, 205101 (2011).
- [10] J.-M. Carter, V. V. Shankar, M. A. Zeb, and H.-Y. Kee, *Phys. Rev. B* **85**, 115105 (2012).
- [11] H.-S. Kim, Y. Chen, and H.-Y. Kee, *Phys. Rev. B* **91**, 235103 (2015).
- [12] Y. Chen, Y.-M. Lu, and H.-Y. Kee, *Nat. Commun.* **6**, 6593 (2015).
- [13] Y. F. Nie, P. D. C. King, C. H. Kim, M. Uchida, H. I. Wei, B. D. Faeth, J. P. Ruf, J. P. C. Ruff, L. Xie, X. Pan *et al.*, *Phys. Rev. Lett.* **114**, 016401 (2015).
- [14] M. Uchida, Y. F. Nie, P. D. C. King, C. H. Kim, C. J. Fennie, D. G. Schlom, and K. M. Shen, *Phys. Rev. B* **90**, 075142 (2014).
- [15] J. Kim, A. H. Said, D. Casa, M. H. Upton, T. Gog, M. Daghofer, G. Jackeli, J. van den Brink, G. Khaliullin, and B. J. Kim, *Phys. Rev. Lett.* **109**, 157402 (2012).
- [16] A. de la Torre, E. C. Hunter, A. Subedi, S. McKeown Walker, A. Tamai, T. K. Kim, M. Hoesch, R. S. Perry, A. Georges, and F. Baumberger, *Phys. Rev. Lett.* **113**, 256402 (2014).
- [17] B.-J. Yang and N. Nagaosa, *Phys. Rev. Lett.* **112**, 246402 (2014).
- [18] K. Fujiwara, Y. Fukuma, J. Matsuno, H. Idzuchi, Y. Niimi, Y. Otani, and H. Takagi, *Nat. Commun.* **4**, 2893 (2013).
- [19] M. Uchida, W. Sano, K. S. Takahashi, T. Koretsune, Y. Kozuka, R. Arita, Y. Tokura, and M. Kawasaki, *Phys. Rev. B* **91**, 241119 (2015).
- [20] E. Varkaraki, J. Nicole, E. Plattner, C. Cominellis, and C. Vayenas, *J. Appl. Electrochem.* **25**, 978 (1995).
- [21] B. H. Meekins and P. V. Kamat, *J. Phys. Chem. Lett.* **2**, 2304 (2011).
- [22] J. M. Rondinelli, S. J. May, and J. W. Freeland, *MRS Bull.* **37**, 261 (2012).
- [23] S. Butler and J. Gillson, *Mater. Res. Bull.* **6**, 81 (1971).
- [24] See Supplemental Material at <http://link.aps.org/supplemental/10.1103/PhysRevB.94.121104> for contains additional film characterization, extraction of the p-d separation, determination of k_z , determination of the quasiparticle residue Z' , and parameters for core level fitting.
- [25] P. Blaha, K. Schwarz, G. K. H. Madsen, D. Kvasnicka, and J. Luitz, *WIEN2K, An Augmented Plane Wave + Local Orbitals Program for Calculating Crystal Properties* (Karlheinz Schwarz, Techn. Universität Wien, Austria, 2001).
- [26] S. K. Panda, S. Bhowal, A. Delin, O. Eriksson, and I. Dasgupta, *Phys. Rev. B* **89**, 155102 (2014).
- [27] J. M. Kahk, C. G. Poll, F. E. Oropeza, J. M. Ablett, D. Céolin, J.-P. Rueff, S. Agrestini, Y. Utsumi, K. D. Tsuei, Y. F. Liao *et al.*, *Phys. Rev. Lett.* **112**, 117601 (2014).
- [28] W. D. Ryden, A. W. Lawson, and C. C. Sartain, *Phys. Rev. B* **1**, 1494 (1970).
- [29] E. A. Nowadnick, J. P. Ruf, H. Park, P. D. C. King, D. G. Schlom, K. M. Shen, and A. J. Millis, *Phys. Rev. B* **92**, 245109 (2015).
- [30] A. Koitzsch, S. V. Borisenko, A. A. Kordyuk, T. K. Kim, M. Knupfer, J. Fink, H. Berger, and R. Follath, *Phys. Rev. B* **69**, 140507 (2004).
- [31] R. Arita, J. Kuneš, A. V. Kozhevnikov, A. G. Eguiluz, and M. Imada, *Phys. Rev. Lett.* **108**, 086403 (2012).
- [32] Y. Taguchi, T. Okuda, M. Ohashi, C. Murayama, N. Môri, Y. Iye, and Y. Tokura, *Phys. Rev. B* **59**, 7917 (1999).
- [33] M. B. Salamon and M. Jaime, *Rev. Mod. Phys.* **73**, 583 (2001).
- [34] K. M. Shen, N. Kikugawa, C. Bergemann, L. Balicas, F. Baumberger, W. Meevasana, N. J. C. Ingle, Y. Maeno, Z.-X. Shen, and A. P. Mackenzie, *Phys. Rev. Lett.* **99**, 187001 (2007).
- [35] R. Burriel, E. F. Westrum, and E. Cordfunke, *J. Chem. Thermodyn.* **19**, 1227 (1987).
- [36] Y. Ishida, R. Eguchi, M. Matsunami, K. Horiba, M. Taguchi, A. Chainani, Y. Senba, H. Ohashi, H. Ohta, and S. Shin, *Phys. Rev. Lett.* **100**, 056401 (2008).

- [37] J. Krempaský, V. N. Strocov, L. Patthey, P. R. Willmott, R. Herger, M. Falub, P. Blaha, M. Hoesch, V. Petrov, M. C. Richter *et al.*, *Phys. Rev. B* **77**, 165120 (2008).
- [38] K. Saeki, T. Wakita, Y. Muraoka, M. Hirai, T. Yokoya, R. Eguchi, and S. Shin, *Phys. Rev. B* **80**, 125406 (2009).
- [39] H.-D. Kim, H.-J. Noh, K. H. Kim, and S.-J. Oh, *Phys. Rev. Lett.* **93**, 126404 (2004).
- [40] Y. Kim, Y. Gao, and S. Chambers, *Appl. Surf. Sci.* **120**, 250 (1997).
- [41] L. F. Mattheiss, *Phys. Rev. B* **13**, 2433 (1976).
- [42] J. Zaanen, G. A. Sawatzky, and J. W. Allen, *Phys. Rev. Lett.* **55**, 418 (1985).
- [43] P. I. Sorantin and K. Schwarz, *Inorg. Chem.* **31**, 567 (1992).
- [44] T. Birol and K. Haule, *Phys. Rev. Lett.* **114**, 096403 (2015).
- [45] B. F. Phelan, J. Krizan, W. Xie, Q. Gibson, and R. J. Cava, *Phys. Rev. B* **91**, 155117 (2015).